

Comparative study of the electronic structure, phonon spectra and electron-phonon interaction of ZrB_2 and TiB_2

S.M. Sichkar,¹ V.N. Antonov,^{1,2} and V.P. Antropov²

¹*Institute of Metal Physics, 36 Vernadsky Street, 03142 Kiev, Ukraine*

²*Ames Laboratory USDOE, Ames, IA 50011*

(Dated: November 27, 2024)

The electronic structure, optical and x-ray absorption spectra, angle dependence of the cyclotron masses and extremal cross sections of the Fermi surface, phonon spectra, electron-phonon Eliashberg and transport spectral functions, temperature dependence of electrical resistivity of the MB_2 ($\text{M}=\text{Ti}$ and Zr) diborides were investigated from first principles using the full potential linear muffin-tin orbital method. The calculations of the dynamic matrix were carried out within the framework of the linear response theory. A good agreement with experimental data of optical and x-ray absorption spectra, phonon spectra, electron-phonon spectral functions, electrical resistivity, cyclotron masses and extremal cross sections of the Fermi surface was achieved.

PACS numbers: 75.50.Cc, 71.20.Lp, 71.15.Rf

I. INTRODUCTION

Ceramics based on transition metal borides, nitrides, and carbides have extremely high melting points ($>2500^\circ\text{C}$) and are referred to as ultra-high temperature ceramics.^{1,2} Among them, diborides such as ZrB_2 and HfB_2 have a unique combination of mechanical and physical properties: high melting points ($>3000^\circ\text{C}$); high thermal and electrical conductivity; chemical inertness against molten metals; great thermal shock resistance.¹⁻³ Thus, although carbides typically have the highest melting points ($>3500^\circ\text{C}$), the diborides ZrB_2 and HfB_2 are more attractive candidates for high-temperature thermomechanical structural applications at temperatures $\geq 3000^\circ\text{C}$.^{1,2} Potential applications include thermal protective structures for leading-edge parts on hypersonic re-entry space vehicles,^{1,4} propulsion systems,^{1,4} furnace elements,⁵ refractory crucibles,⁵ and plasma-arc electrodes.^{5,6} In particular, ZrB_2 has the lowest theoretical density among the ultra-high temperature ceramics, which makes it an attractive material for aerospace applications.^{1,2,4} Titanium diboride is also potentially useful because it has many interesting physical properties, such as low density and unusual strength.⁷ TiB_2 is widely accepted for applications including microelectronics, diffusion barriers, wear- and erosion-resistant coatings for cutting tools and other mechanical components. In these applications, the material's high hardness, high melting point, good electrical conductivity, and acid and radiation stability is exploited.⁸

The discovery of superconductivity in MgB_2 at 39 K by Akimitsu⁹ has lead to booming activity in the physics community and activated a search for superconductivity in other diborides. Natural candidates for this search are AB_2 -type light metal diborides ($\text{A} = \text{Li}, \text{Be}, \text{Al}$). However, up to now superconductivity has not been reported in the majority of these compounds.¹⁰ Only very recently has superconductivity below 1 K ($T_c = 0.72\text{ K}$) been reported in $\text{BeB}_{2.75}$.¹¹ According to Ref. 12 no supercon-

ducting transition down to 0.42 K has been observed in powders of diborides of transition metals ($\text{A} = \text{Ti}, \text{Zr}, \text{Hf}, \text{V}, \text{Ta}, \text{Cr}, \text{Mo}, \text{U}$). Only NbB_2 is expected to superconduct with a rather low transition temperature ($< 1\text{ K}$), and contradictory reports about superconductivity up to $T_c=9.5\text{ K}$ in TaB_2 can be found in Ref. 12. Finally, the reported $T_c=7\text{ K}$ in ZrB_2 ¹⁰ encourages further studies of these diborides.

Presently, a number of experimental studies exist dealing with the physical properties of ZrB_2 and TiB_2 such as electric transport properties,^{7,13-17} the de Haas-van Alphen (dHvA) measurements of the Fermi surface,¹⁸⁻²¹ optical²²⁻²⁴ and electron-energy-loss spectra,^{25,26} x-ray absorption and photoemission spectra,^{27,28} magnetic susceptibility^{29,30} and NMR measurements,³¹ the phonon density of states,³² and electron-phonon interaction.^{32,33} First-principles calculations of the electronic structure of diborides have been widely presented.^{25-27,30,34-51}

Despite a lot of publications, there are still many open questions related to the electronic structure and physical properties of transition metal diborides. Ihara *et al.*²⁷ calculated the band structure and the density of states (DOS) of ZrB_2 by using an augmented plane wave method. They pointed out that the band structure of ZrB_2 is determined by the sp^2 hybridization, p_z state of B and the $4d$ and $5s$ states of Zr. Similarly Johnson³⁴ calculated the band structure of ZrB_2 using the Korringa-Kohn-Rostoker method in the spherical muffin-tin approximation. However, they concluded that the B $2s$ states are localized and do not hybridize with B $2p$. Pablo *et al.*³⁹ compared the electronic structure of isostructural alkaline-earth diborides using a full-potential linearized augmented plane wave (FLAPW) method and found that Zr-B bonds have covalent character, yet still remain highly ionic. Fermi surfaces and DOS values at the Fermi level reported by Shein *et al.*⁴⁰ and those by Rosner *et al.*³⁸ are quite different. Vajeeston *et al.*³⁷ also investigated the electronic structure of AlB_2 -type diborides using the tight-binding linear muffin-tin orbital

(TB-LMTO) method, they claimed that metal-metal and metal-boron interactions are less significant than the p - p covalent interaction of boron atoms. Burdett *et al.*,³⁵ on the basis of orbital overlap, indicated the importance of the interaction of orbitals of the metal with those of a graphite-like net of boron atoms as well as the interaction with those of other metals in influencing the properties of these species. The bonding nature, elastic property and hardness were investigated by Zhang *et al.*⁴⁷ for ZrB_2 using the plane-wave pseudopotential method. The stiffness and the thermal expansion coefficient of ZrB_2 were calculated using the density functional theory formalism by Milman *et al.* in Ref. 52. Kaur *et al.*⁵³ studied the cohesive and thermal properties of these compounds using the rigid ion model. The elastic properties, electronic structure, electronic charge distribution, and equation of states of titanium diboride were studied by Milman and Warren,⁵⁴ Perottoni *et al.*,⁵⁵ and Camp *et al.*⁵⁶ using the first-principles methods. Peng *et al.*⁵⁷ investigated the thermodynamic properties of TiB_2 using a plane-wave pseudopotential method. Munro⁸ examined the physical, mechanical, and thermal properties of polycrystalline TiB_2 and showed that these properties are significantly related to the density and grain size of the used specimens. Deligoz *et al.*^{48,50} investigated the structural and lattice dynamical properties of TiB_2 and ZrB_2 together with VB_2 , ScB_2 , NbB_2 , and MoB_2 . They specifically presented following properties: lattice parameters; bond lengths; phonon dispersion curves and corresponding density of states; some thermodynamic quantities such as internal energy, entropy, heat capacity, and their temperature-dependent behaviors. Systematic trends in lattice constants and heats of formation for these compounds were studied by Oguchi.⁵⁸ Vajeeston *et al.*³⁷ investigated the electronic structure and ground state properties of these diborides using TB-LMTO. X-ray absorption and photoemission spectra of ZrB_2 and TiB_2 were measured experimentally in Refs. 27,28,59. The optical spectra of ZrB_2 was investigated experimentally by several authors,²²⁻²⁴ however, there is neither theoretical investigation of the x-ray absorption spectra or the optical properties of the transition metal diborides.

The band structure and Fermi surface parameters were studied by Shein and Ivanovskii⁴⁰ using the self-consistent full potential linearized muffin-tin orbital (FP-LMTO) method for ZrB_2 and NbB_2 . Rosner *et al.*^{38,43} provided a comparison of full potential band calculations of the Fermi surfaces areas and masses of MgB_2 and ZrB_2 with dHvA data for several symmetry points in the Brillouin zone (BZ). They found, with one possible exception, that LDA provides a good description for ZrB_2 . For MgB_2 some disagreement in FS areas can be accounted for by a shift of π ($B p_z$) bands with respect to σ ($B sp_x p_y$) bands by 240 meV and by a readjustment of the "Fermi energies" of each of these bands by ± 120 meV. Heid *et al.*³² measured the phonon density of states of MB_2 with $M=\text{Ti, V, Ta, Nb, and Y}$ using inelastic neutron scattering. Experimental data were compared with

ab initio density-functional calculations using the mixed basis pseudopotential method. The results do not exhibit indications of strong electron-phonon interaction in the diborides considered. Singh⁴² studied electron-phonon interaction in ZrB_2 and TaB_2 using a FP-LMTO method. The results for phonon density of states and Eliashberg function show electron-phonon coupling in ZrB_2 to be much weaker than in TaB_2 . The average electron-phonon coupling constant λ is found to be 0.15 for ZrB_2 and 0.73 for TaB_2 . Solutions of the isotropic Eliashberg gap equation indicate no superconductivity for ZrB_2 .

The aim of this work is a complex comparative investigation of the electronic structure, optical and x-ray absorption spectra, angle dependence of the cyclotron masses and extremal cross sections of the Fermi surface, phonon spectra, electron-phonon interaction and electrical resistivity of the diborides TiB_2 and ZrB_2 . The paper is organized as follows. Section II presents the details of the calculations. Section III is devoted to the electronic structure as well as optical and x-ray absorption spectra, angle dependence of the cyclotron masses and extremal cross sections of the Fermi surface, phonon spectra, electron-phonon interaction and electrical resistivity using the FP-LMTO band structure method. The results are compared with available experimental data. Finally, the results are summarized in Sec. IV.

II. COMPUTATIONAL DETAILS

Most known transition-metal (M) diborides MB_2 are formed by group III-VI transition elements (Sc, Ti, Zr, Hf, V, Nb, and others) and have a layered hexagonal C32 structure of the AlB_2 -type with the space group symmetry $P6/mmm$ (number 191). It is simply a hexagonal lattice in which closely-packed transition metal layers are present alternative with graphite-like B layers (Fig. 1). These diborides cannot be exactly layered compounds because the inter-layer interaction is strong even though the M layers alternate with the B layers in their crystal structure. The boron atoms lie on the corners of hexagons with the three nearest neighbor boron atoms in each plane. The M atoms lie directly in the centers of each boron hexagon, but midway between adjacent boron layers. Each transition metal atom has twelve nearest neighbor B atoms and eight nearest neighbor transition metal atoms (six are on the metal plane and two out of the metal plane). There is one formula unit per primitive cell and the crystal has simple hexagonal symmetry ($D6h$). By choosing appropriate primitive lattice vectors, the atoms are positioned at M (0,0,0), B ($\frac{1}{3}, \frac{1}{6}, \frac{1}{2}$), and B ($\frac{2}{3}, \frac{1}{3}, \frac{1}{2}$) in the unit cell. The distance between M-M is equal to c . This structure is quite close packed, and can be coped with efficiently and accurately by the atomic sphere approximation method. However, for precise calculation of the phonon spectra and electron-phonon interaction, a full potential approximation should be used.

For a crystal where both the fourfold axis and the mag-

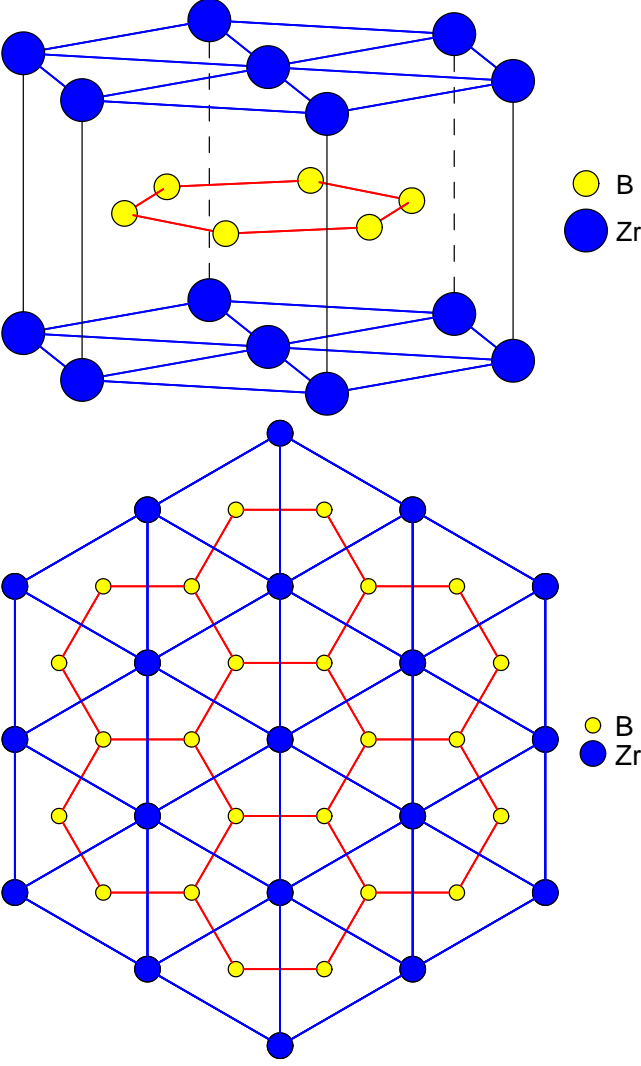


FIG. 1: (Color online) Schematic representation of the ZrB_2 structure (upper panel) and top view of Zr (large blue circles) and B (small yellow circles) planes in ZrB_2 (lower panel).

netization \mathbf{M} are perpendicular to the sample surface, and the z -axis is chosen to be parallel to them, the dielectric tensor is composed of the diagonal ε_{xx} and ε_{zz} , and the off-diagonal ε_{xy} components in the form⁶⁰

$$\varepsilon = \begin{pmatrix} \varepsilon_{xx} & \varepsilon_{xy} & 0 \\ -\varepsilon_{xy} & \varepsilon_{xx} & 0 \\ 0 & 0 & \varepsilon_{zz} \end{pmatrix}. \quad (1)$$

The various elements $\hat{\varepsilon}_{\alpha\beta}$ are composed of real and imaginary parts as follows: $\hat{\varepsilon}_{\alpha\beta} = \varepsilon_{\alpha\beta}^{(1)} + i\varepsilon_{\alpha\beta}^{(2)}$, where $\alpha, \beta \equiv x, y, z$; $\varepsilon_{xx} = (n + ik)^2$; n and k are the refractive index and extinction coefficient, respectively. The optical conductivity tensor $\hat{\sigma}_{\alpha\beta} = \sigma_{\alpha\beta}^{(1)} + i\sigma_{\alpha\beta}^{(2)}$ is related to the

dielectric tensor $\varepsilon_{\alpha\beta}$ through the equation

$$\hat{\varepsilon}_{\alpha\beta}(\omega) = \delta_{\alpha\beta} + \frac{4\pi i}{\omega} \hat{\sigma}_{\alpha\beta}(\omega). \quad (2)$$

The optical conductivity of ZrB_2 and TiB_2 has been computed from the energy band structure by means of the Kubo-Greenwood⁶¹ linear-response expression:⁶²

$$\sigma_{\alpha\beta}(\omega) = \frac{-ie^2}{m^2 \hbar V_{uc}} \times \sum_{\mathbf{k}} \sum_{nn'} \frac{f(\epsilon_{n\mathbf{k}}) - f(\epsilon_{n'\mathbf{k}})}{\omega_{nn'}(\mathbf{k})} \frac{\Pi_{nn'}^\alpha(\mathbf{k}) \Pi_{nn'}^\beta(\mathbf{k})}{\omega - \omega_{nn'}(\mathbf{k}) + i\gamma} \quad (3)$$

where $f(\epsilon_{n\mathbf{k}})$ is the Fermi function; $\hbar\omega_{nn'}(\mathbf{k}) \equiv \epsilon_{n\mathbf{k}} - \epsilon_{n'\mathbf{k}}$ is the energy difference of Kohn-Sham energies; γ is the lifetime parameter, describing the finite lifetime of the excited Bloch electron states; $\Pi_{nn'}^\alpha$ are the dipole optical transition matrix elements.⁶⁰ A detailed description of the optical matrix elements is given in Refs. 60,63. The absorptive part of the optical conductivity was calculated in a wide energy range. The Kramers-Kronig transformation was then used to calculate the dispersive parts of the optical conductivity from the absorptive part. We used the value $\gamma=0.6$ eV for the interband relaxation parameter.

Within the one-particle approximation, the absorption coefficient $\mu_\lambda^j(\omega)$ for incident x-ray of polarization λ and photon energy $\hbar\omega$ can be determined as the probability of electronic transitions from initial core states with the total angular momentum j to final unoccupied Bloch states

$$\mu_\lambda^j(\omega) = \sum_{m_j} \sum_{n\mathbf{k}} |\langle \Psi_{n\mathbf{k}} | \Pi_\lambda | \Psi_{jm_j} \rangle|^2 \delta(E_{n\mathbf{k}} - E_{jm_j} - \hbar\omega) \times \theta(E_{n\mathbf{k}} - E_F), \quad (4)$$

where Ψ_{jm_j} and E_{jm_j} are the wave function and the energy of a core state with the projection of the total angular momentum m_j ; $\Psi_{n\mathbf{k}}$ and $E_{n\mathbf{k}}$ are the wave function and the energy of a valence state in the n -th band with the wave vector \mathbf{k} ; ε_F is the Fermi energy.

Π_λ is the electron-photon interaction operator in the dipole approximation

$$\Pi_\lambda = -e\boldsymbol{\alpha}\mathbf{a}_\lambda, \quad (5)$$

where $\boldsymbol{\alpha}$ are the Dirac matrices, \mathbf{a}_λ is the λ polarization unit vector of the photon vector potential, with $a_\pm = 1/\sqrt{2}(1, \pm i, 0)$, $a_\parallel = (0, 0, 1)$. Here, $+$ and $-$ denotes, respectively, the left and right circular photon polarizations with respect to the magnetization direction in the solid. Then, x-ray magnetic circular and linear dichroism are given by $\mu_+ - \mu_-$ and $\mu_\parallel - (\mu_+ + \mu_-)/2$, respectively. More detailed expressions of the matrix elements for the spin-polarized fully relativistic LMTO method may be found in Refs. 63,64.

The Eliashberg function (the spectral function of the electron-phonon interaction) expressed in terms of the phonon linewidths $\gamma_{\mathbf{q}\nu}$ has the form⁶⁵

$$\alpha^2 F(\omega) = \frac{1}{2\pi N(\epsilon_F)} \sum_{\mathbf{q}\nu} \frac{\gamma_{\mathbf{q}\nu}}{\omega_{\mathbf{q}\nu}} \delta(\omega - \omega_{\mathbf{q}\nu}), \quad (6)$$

The line-widths characterize the partial contribution of each phonon:

$$\gamma_{\mathbf{q}\nu} = 2\pi\omega_{\mathbf{q}\nu} \sum_{jj'\mathbf{k}} |g_{\mathbf{k}+\mathbf{q}j',\mathbf{k}j}^{\mathbf{q}\nu}|^2 \delta(\epsilon_{j\mathbf{k}} - \epsilon_F) \delta(\epsilon_{\mathbf{k}+\mathbf{q}j'} - \epsilon_F). \quad (7)$$

The electron-phonon interaction constant is defined as:

$$\lambda_{e-ph} = 2 \int_0^\infty \frac{d\omega}{\omega} \alpha^2 F(\omega), \quad (8)$$

It can also be expressed in terms of the phonons line-widths:

$$\lambda_{e-ph} = \sum_{\mathbf{q}\nu} \frac{\gamma_{\mathbf{q}\nu}}{\pi N(\epsilon_F) \omega_{\mathbf{q}\nu}^2}, \quad (9)$$

were $N(\epsilon_F)$ is the electron density of states per atom and per spin on the Fermi level (ϵ_F) and $g_{\mathbf{k}+\mathbf{q}j',\mathbf{k}j}^{\mathbf{q}\nu}$ is the electron-phonon interaction matrix element. The double summation over Fermi surface in Eq.(7) was carried out on dense mesh (793 point in the irreducible part of the BZ)

Calculations of the electronic structure and physical properties of the TiB_2 and ZrB_2 diborides were performed using a scalar relativistic FP-LMTO method⁶⁶ with the experimentally observed lattice constants: $a=3.167 \text{ \AA}$ and $c=3.529 \text{ \AA}$ for ZrB_2 ;⁶⁷ $a=3.03 \text{ \AA}$ $c=3.229 \text{ \AA}$, for TiB_2 .⁶⁸ For the LMTO calculations we used the Perdew-Wang⁶⁹ parameterization of the exchange-correlation potential in general gradient approximation. BZ integrations were performed using the improved tetrahedron method.⁷⁰ Phonon spectra and electron-phonon matrix elements were calculated for 50 points in the irreducible part of the BZ using the linear response scheme developed by Savrasov.⁶⁶ The $3s$ and $3p$ semi-core states of TiB_2 were treated as valence states in separate energy windows (for ZrB_2 : $4s$ and $4p$). Variations in charge density and potential were expanded in spherical harmonics inside the MT sphere as well as 2894 plane waves in the interstitial area with 88.57 Ry cut-off energy for ZrB_2 and 97.94 Ry cut-off energy for TiB_2 . As for the area inside the MT spheres, we used $3k\text{--}spd$ LMTO basis set energy (-0.1, -1, -2.5 Ry) with one-center expansions inside the MT-spheres performed up to $l_{max} = 6$.

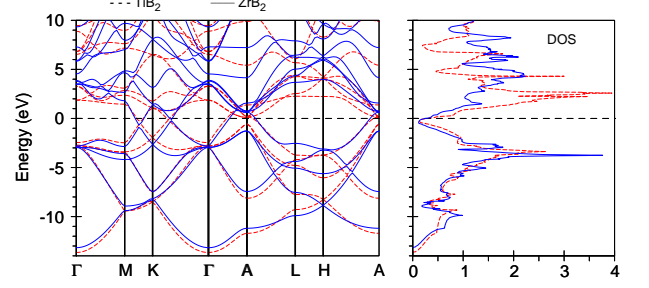


FIG. 2: (Color online) Energy band structure and total DOS [in states/(cell eV)] of ZrB_2 (full blue lines) and TiB_2 (dashed red lines).

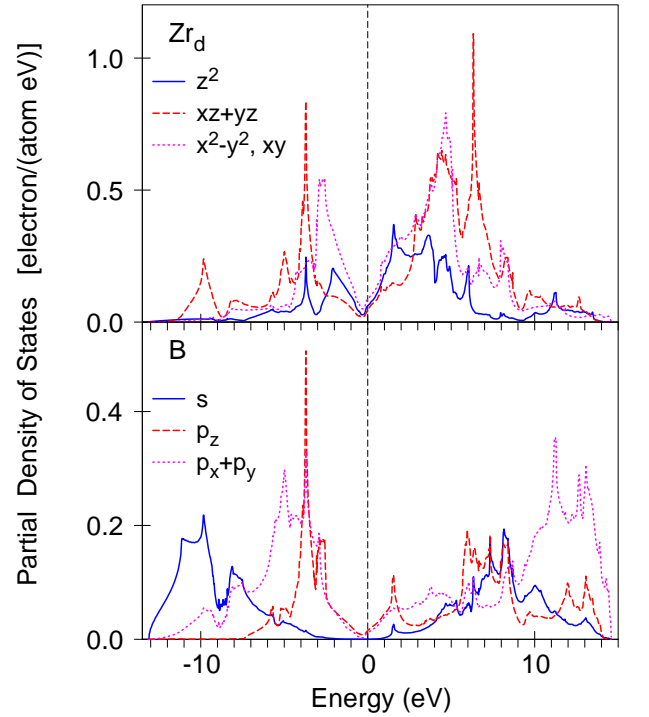


FIG. 3: (Color online) Partial DOSs [in states/(atom eV)] of ZrB_2 .

III. RESULTS AND DISCUSSION

A. Energy band structure

Figure 2 presents the energy band structure and total density of states (DOS) of ZrB_2 (full lines) and TiB_2 (dashed lines). The partial DOSs ZrB_2 are shown in Fig. 3. Our results for the electronic structure of ZrB_2 and TiB_2 are in agreement with earlier calculations.^{29,30,42,48–51} A common feature for all transition metal diborides is the deep DOS minimum (pseudo-gap) at the Fermi energy separating the valence band and the conduction band. According to Pasturel *et al.*,⁷¹ a pseudo-gap arises because of a strong chemical inter-

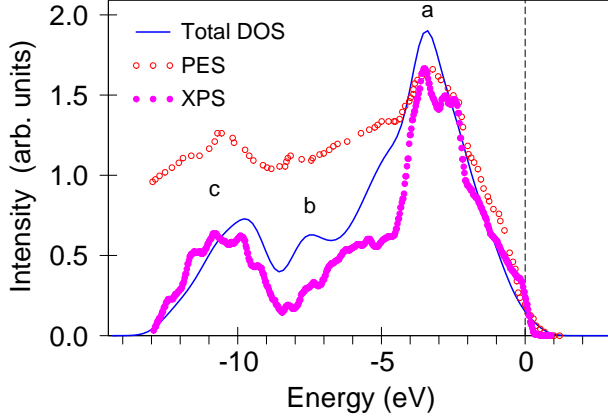


FIG. 4: (Color online) Comparison of the total DOS (full line) with photoemission²⁸ (open circles) and x-ray photoemission²⁷ (full circles) of ZrB₂.

action. The M-B covalent bonding is believed to be responsible for this effect. Fig. 2 includes a comparison of the total DOS for ZrB₂ and TiB₂. In both systems, we observe a deep minimum in the DOS at the Fermi energy, although the gap appears slightly broader in the case of ZrB₂. The Zr 4*d* states in ZrB₂ are the dominant features in the interval from -12.5 eV to 9 eV. These tightly bound states show overlap with B 2*p* and, to a lesser extent, with B 2*s* states both above and below ε_F , implying considerable covalency. Higher-energy states between 9 eV and 20 eV above ε_F appear to arise from Zr 5*p* and 6*s* states hybridized with B 2*p* states. The crystal field at the Zr site (*D*6*h* point symmetry) causes the splitting of Zr *d* orbitals into a singlet a_{1g} (d_{3z^2-1}) and two doublets e_{1g} (d_{yz} and d_{xz}) and e_{2g} (d_{xy} and $d_{x^2-y^2}$). The crystal field at the B site (*D*3*h* point symmetry) causes the splitting of B *p* orbitals into a singlet a_4 (p_z) and a doublet e_2 (p_x and p_y). B *s* states occupy a bottom of valence band between -13.1 eV and -3.0 eV and hybridize strongly with B p_x and p_y and Zr d_{yz} and d_{xz} states located at -12.5 eV to -0.5 eV. B p_x and p_y states are located between -12.5 eV and -0.5 eV. B p_z states occupied a smaller energy interval from -7.5 eV to -0.5 eV with a very strong and narrow peak structure at around -4 eV.

B. X-ray absorption and photoemission spectra

Experimentally the electronic structure of ZrB₂ and TiB₂ has been investigated by means of photoemission spectroscopy,^{27,28} point contact spectroscopy,³³ x-ray absorption spectroscopy,^{28,59} and optical spectroscopy.²²⁻²⁴

Figure 4 shows the experimentally measured photoemission (PES)²⁸ and x-ray photoemission (XPS)²⁷ spectra of ZrB₂ compared with the calculated energy distribution of total DOS. The calculated DOS has been broadened to account for life-time effects and for the

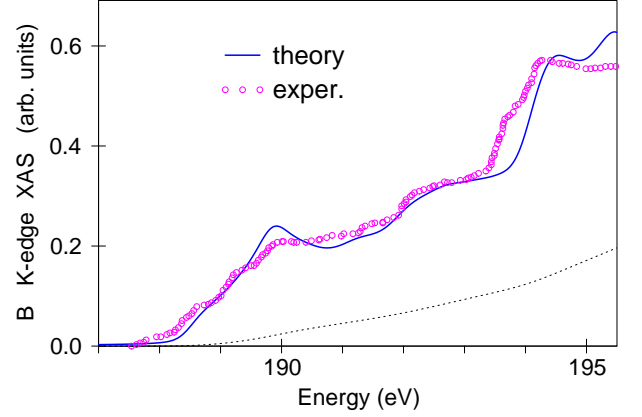


FIG. 5: (Color online) The theoretically calculated and experimentally measured²⁸ x-ray absorption spectra at B *K* edge of ZrB₂.

experimental resolution. The characteristic features of the XPS are divided into three parts ranging from the Fermi energy to -4.5 eV (peak *a*), -4.5 eV to -8.5 eV (peak *b*), and -8.5 eV to -13 eV (peak *c*). The low energy peak *c* arises mostly from the B 2*s* states and partly from the low energy peak of Zr 4*d*_{*xz,yz*} states (see Fig. 3). The major peak *a* close to the Fermi energy is derived by Zr 4*d* states. B *p* states as well as the Zr 4*d*_{*xz,yz*} states contribute to the broad peak *c* located from -4.5 eV to -8.5 eV. Agreement between experiment and theory in energy position of major fine structures is reasonably well. However, peak *b* is slightly shifted toward lower energy in the theory, besides, peak *a* does not split into two peaks as observed in the experimental XPS spectrum. On the other hand, the experimental PE spectrum²⁸ measured at 325.26 eV (open circles in Fig. 4) has a single peak *a* in close agreement with the theoretically calculated DOS. Intensity of the low energy part of the PE spectrum is significantly increased due to inelastically scattered electrons. The corresponding background was extracted from the experimental XPS spectrum.²⁷ It is interesting to note that the position of the peak *b* in DOS is in better agreement with the PE spectrum than observed in the case of the XPS spectrum.

X-ray absorption spectra (XAS) were measured by Tsuda *et al.*²⁸ at the B *K* and Zr *M*_{2,3} edges of ZrB₂. Ti *K* XAS were measured by Chu *et al.*⁵⁹ The XA spectra in metals at the *K* edge in which the 1*s* core electrons are excited to the *p* states through the dipolar transition usually attract only minor interest because *p* states are not the states of influencing magnetic or orbital order. Recently, however, understanding *p* states has become important due to XA spectroscopy using *K* edges of transition metals gaining popularity. The *K* edge XAS is sensitive to electronic structures at neighboring sites because of the delocalized nature of the *p* states.

Figure 5 presents the theoretically calculated and experimentally measured B *K* XPS spectra (1*s* → 2*p* tran-

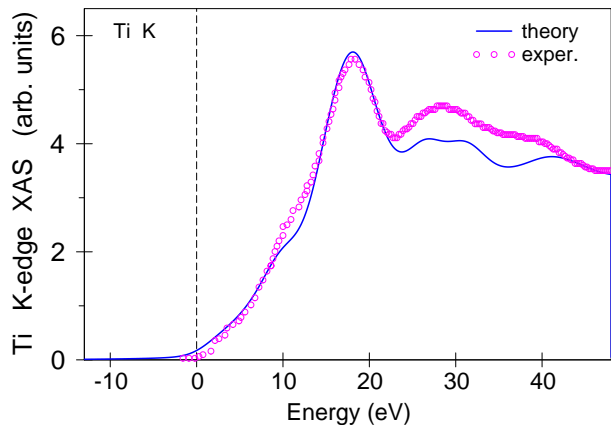


FIG. 6: (Color online) The theoretically calculated and experimentally measured⁵⁹ x-ray absorption spectra at Ti K edge of TiB_2 .

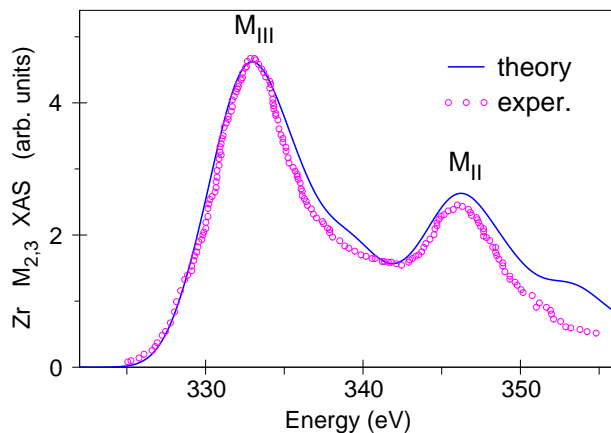


FIG. 7: (Color online) The theoretically calculated and experimentally measured²⁸ x-ray absorption spectra at Zr $M_{2,3}$ edges of ZrB_2 .

sitions). The agreement between the theory and the experiment is excellent. The low energy peak around 190 eV is due to transitions from the $1s$ core level to the mostly B p_z states (see Fig. 3) with some amount of the p_x and p_y states. Fine structure at 194.5 eV reflects the corresponding peak between 6 eV and 7 eV above the Fermi level (Fig. 3). Figure 6 presents theoretically calculated and experimentally measured⁵⁹ Ti K XPS spectra in TiB_2 . The agreement between theory and experiment is also quite good; except for a second major peak around 28 eV that is slightly underestimated theoretically.

Figure 7 presents theoretically calculated and experimentally measured Zr $M_{2,3}$ XPS spectra ($3p \rightarrow 4d$ transitions). Agreement between theory and experiment is again good. Because of the dipole selection rules (apart from the $4s_{1/2}$ -states that which have a small contribution to the XAS due to relatively small $3p \rightarrow 5s$ matrix

elements⁶⁰) only $3d_{3/2}$ -states occur as final states for M_2 XAS. For the M_3 XAS, $4d_{5/2}$ -states also contribute. Although the $3p_{3/2} \rightarrow 4d_{3/2}$ radial matrix elements are only slightly smaller than for the $3p_{3/2} \rightarrow 4d_{5/2}$ transitions, the angular matrix elements strongly suppress the $3p_{3/2} \rightarrow 4d_{3/2}$ contribution.⁶⁰ Therefore in neglecting the energy dependence of the radial matrix elements, the M_2 and the M_3 spectra can be viewed as a direct mapping of the DOS curve for $4d_{3/2}$ - and $4d_{5/2}$ -character, respectively.

C. Optical spectra

The optical spectra of ZrB_2 have been measured by several authors.^{22–24} Currently there are no such measurements for TiB_2 . Fig. 8 shows the theoretically calculated and experimentally measured optical reflectivity spectra $R(\omega)$ as well as dielectric constants $\epsilon_1(\omega)$ and $\epsilon_2(\omega)$ for ZrB_2 . Also presented are theoretically calculated $R(\omega)$, $\epsilon_1(\omega)$, and $\epsilon_2(\omega)$ for TiB_2 . Theory reproduces well peculiarities of ZrB_2 optical spectra.

We performed decomposition of the calculated ϵ_2 spectrum into the contributions arising from separate interband transitions and different places of \mathbf{k} space. We found that the major peak in the $\epsilon_2(\omega)$ (around 1 eV) is mostly determined by the $5 \rightarrow 6$ interband transitions along the Γ –A and A–L symmetry directions (Fig. 9). The shoulder at 2 eV is due to the $4 \rightarrow 5$ interband transitions around A symmetry point (pink dotted lines in Fig. 9).

Although the band structures ZrB_2 and TiB_2 are very similar (see Fig. 2), their optical spectra visibly differ from each other. The experimental measurements of the optical spectra of TiB_2 are highly desirable.

D. Fermi surface

The magnetoresistance and Hall effect were measured in early investigations of the Fermi surface (FS) of ZrB_2 in 1966 by Piper.⁷² He showed that ZrB_2 is a compensated semimetal with an effective concentration of 0.04 electrons/cell with no open trajectories. In 1978, the dHvA effect was observed and investigated by Tanaka *et al.*¹⁸ and an attempt was made to interpret the dHvA oscillations on the basis of calculations of the band structure of CrB_2 ⁷³ using the "rigid band" approximation. The model obtained for the FS of ZrB_2 was later confirmed by improved calculations performed using the FLAPW method.³⁸ Recently the Fermi surfaces of ScB_2 , ZrB_2 and HfB_2 , were studied by Pluzhnikov *et al.*²¹ using the dHvA effect. Their results for ZrB_2 are similar to previous measurements by Tanaka.¹⁸

Theoretical calculations show a ring-like electron FS around the K symmetry point (Fig. 10) and of a wrinkled dumbbell-like hole FS at the A point (Fig. 11) in ZrB_2 . The electron FS and hole FS have threefold and sixfold

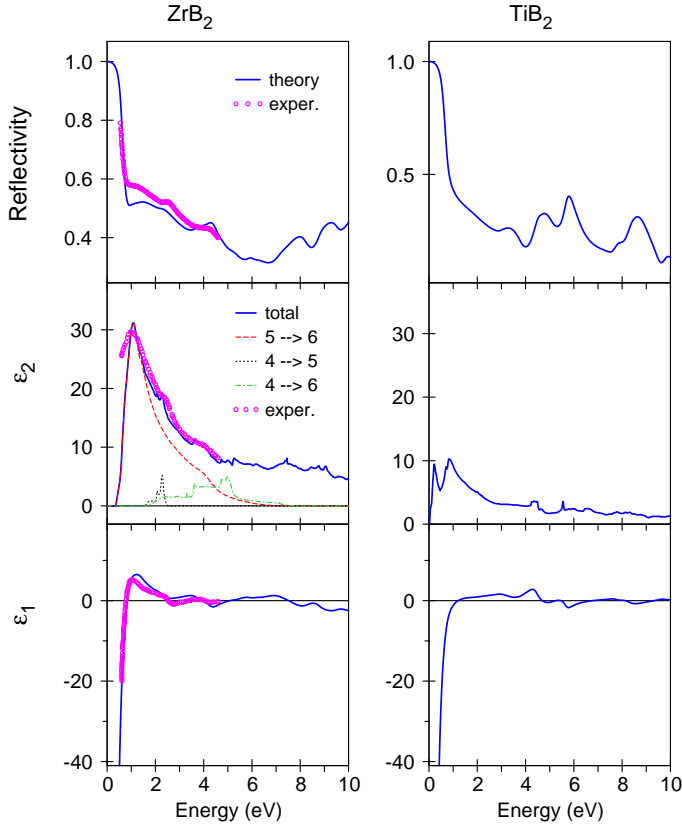


FIG. 8: (Color online) Theoretically calculated (solid blue lines) and experimentally measured (open circles)²⁴ optical reflectivity spectra (upper panel) and dielectric constants ϵ_2 (middle panel) and ϵ_1 (lower panel) of ZrB_2 . For the ϵ_1 function the contributions of different interband transitions are presented.

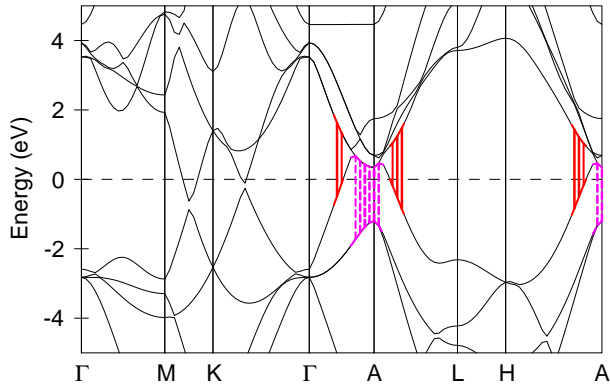


FIG. 9: (Color online) Theoretically calculated $4 \rightarrow 5$ (pink dotted lines) and $5 \rightarrow 6$ (red full lines) interband transitions in the optical conductivity of ZrB_2 .

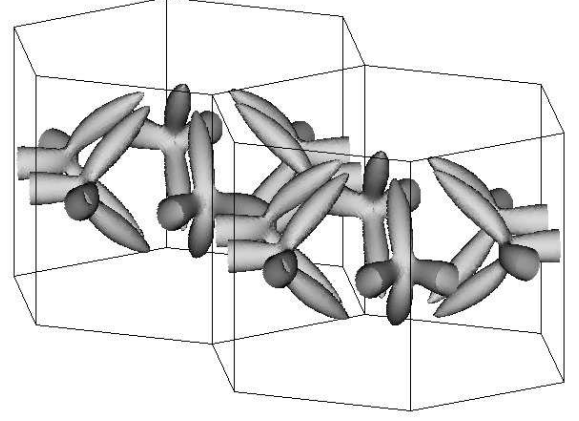


FIG. 10: (Color online) The calculated electron sheets of the Fermi surface around K symmetry point from the 6th energy band of ZrB_2 .

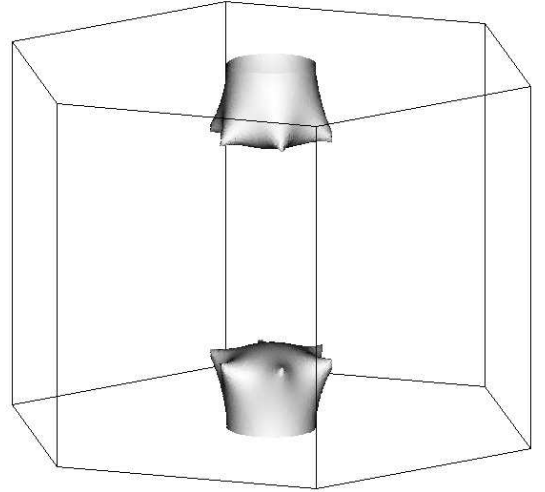


FIG. 11: The calculated hole sheets of the Fermi surface at the A symmetry point from the 5th energy band of ZrB_2 .

symmetries, respectively. These are broadly consistent with the Fermi surfaces used by Tanaka¹⁸ to interpret their dHvA data. TiB_2 has very similar sheets of its Fermi surface.

Figure 12 shows the calculated cross section areas in the plane perpendicular z direction and crossed A symmetry point for hole FS (upper panel) and Γ point for

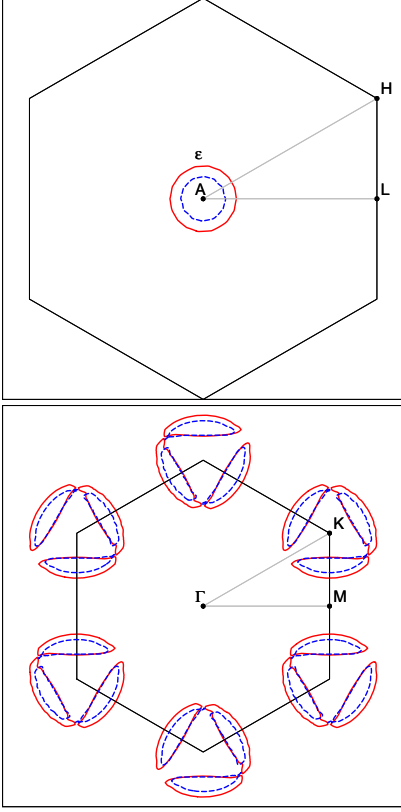


FIG. 12: (Color online) The calculated cross sections in the plane perpendicular z direction and crossed A symmetry point (upper panel) and Γ point (lower panel) for ZrB_2 (full red curves) and TiB_2 (dashed blue curves). The labels are provided as used in the text.

electron FS (lower panel) of ZrB_2 and TiB_2 . It can be clearly seen that TiB_2 has a smaller FS than ZrB_2 .

Figure 13 represents angular variations of the experimentally measured dHvA frequencies²¹ for ZrB_2 in comparison with the first-principle calculations for field direction in the $(10\bar{1}0)$, $(11\bar{2}0)$, and (0001) planes. The observed frequencies of α , β , γ , and δ oscillations belong to electron FS around the K point (see Fig. 4 in Ref. 18). The ϵ , ν , μ , and ζ orbits belong to the hole wrinkled dumbbell FS. The α frequencies have four branches at the $(10\bar{1}0)$ plane and three branches at the $(11\bar{2}0)$ plane. The lower γ frequencies have two branches in both the planes.

The theory reasonably well reproduces the frequencies measured experimentally. However, there are still some discrepancies. For high frequencies in the $<0001>$ direction, we found the ϵ and μ branches but were unable to obtain ν branch. We also discover a new branch σ which is not detected experimentally. This branch belongs to the electron FS around the K point. It has almost a constant frequency at the $(10\bar{1}0)$ plane and rapidly drops in frequency at the (0001) plane. The theoretically calculated ζ orbits exist in a wider angle interval than observed experimentally.

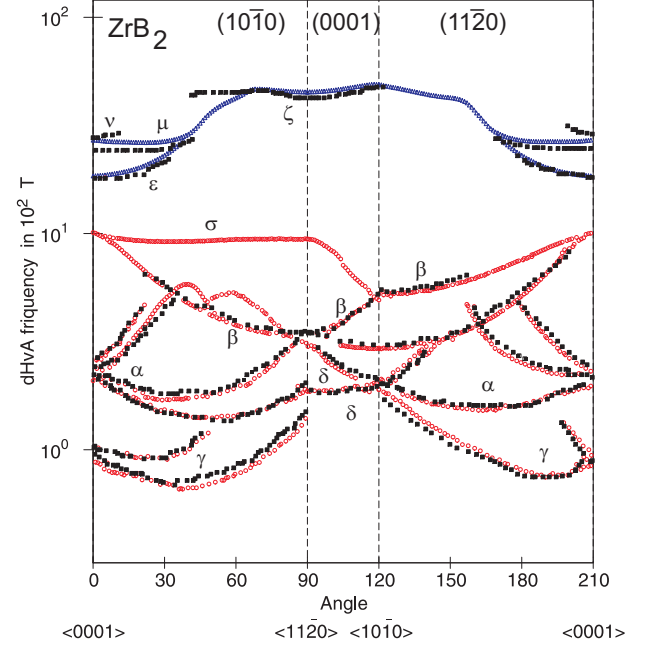


FIG. 13: (Color online) The calculated (open red and blue circles for the electron and hole surfaces, respectively) and experimentally measured²¹ (black full squares) angular dependence of the dHvA oscillation frequencies in the compound ZrB_2 .

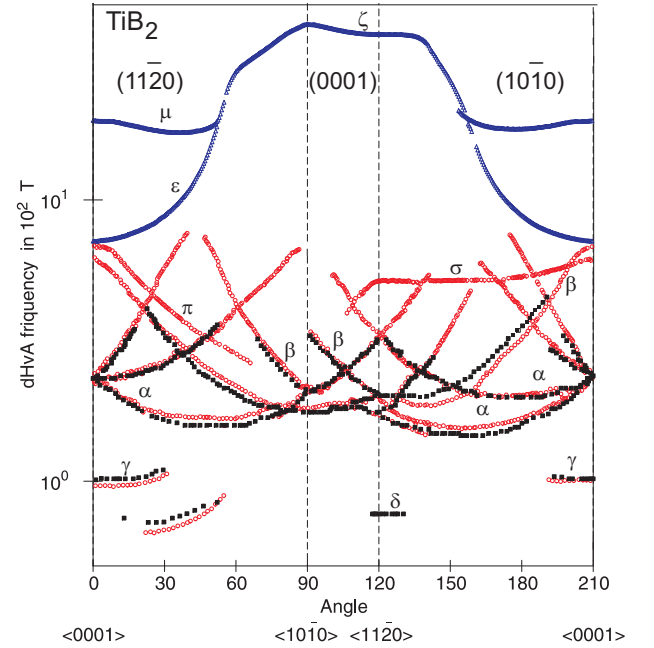


FIG. 14: (Color online) The calculated (open red and blue circles for the electron and hole surfaces, respectively) and experimentally measured²⁰ (black full squares) angular dependence of the dHvA oscillation frequencies in the compound TiB_2 .

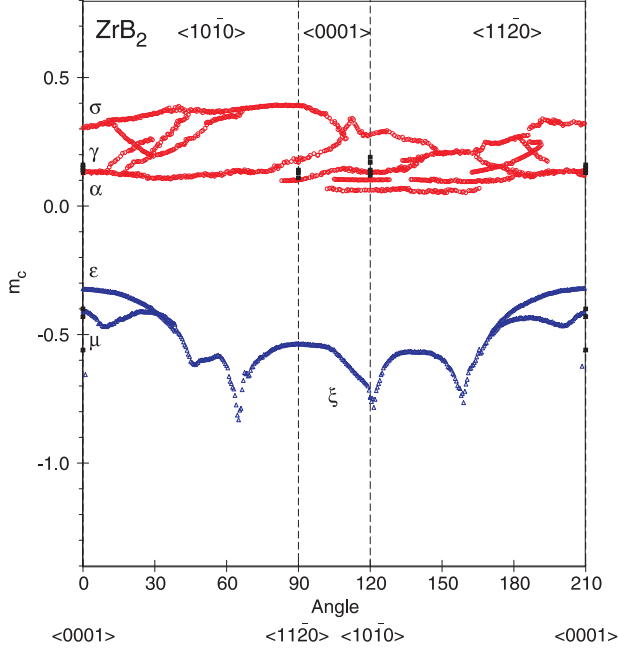


FIG. 15: (Color online) The calculated angular dependence of the cyclotron masses for the electron Fermi surface (open red circles) and the hole Fermi surface (blue open triangles) and experimentally measured ones (black full squares) in the compound ZrB_2 .

Figure 14 represents an angular variation of experimentally measured dHvA frequencies²⁰ in TiB_2 when compared with theoretically calculated frequencies. The theoretical calculations quite well reproduce the angle dependence of the extremal cross sections for low frequency orbits γ , α and β . Similar to ZrB_2 we detected theoretically a new branch σ in TiB_2 which is not observed experimentally. This branch belongs to the electron FS around the K point. We also find an additional orbit π at the $(11\bar{2}0)$ plane which is absent in ZrB_2 and did not detected experimentally. We were not able to find theoretically low frequency δ oscillations appeared in a small angle interval near the $\langle 11\bar{2}0 \rangle$ direction. For high frequencies we found the ϵ , μ and ζ branches similar to the corresponding orbits in ZrB_2 . However, these orbits have not been detected in the dHvA experiment.²⁰ One of the possible reasons for that is the relatively large cyclotron masses for these orbits. Figures 15 and 16 show the calculated angular dependence of the cyclotron masses for ZrB_2 and TiB_2 , respectively. The cyclotron masses for the ϵ , μ , and ζ orbits in TiB_2 are much higher than the corresponding orbits in ZrB_2 . The masses for the low-frequency oscillations α , β , γ and δ are less than $0.2m_0$ for ZrB_2 and slightly larger in TiB_2 .

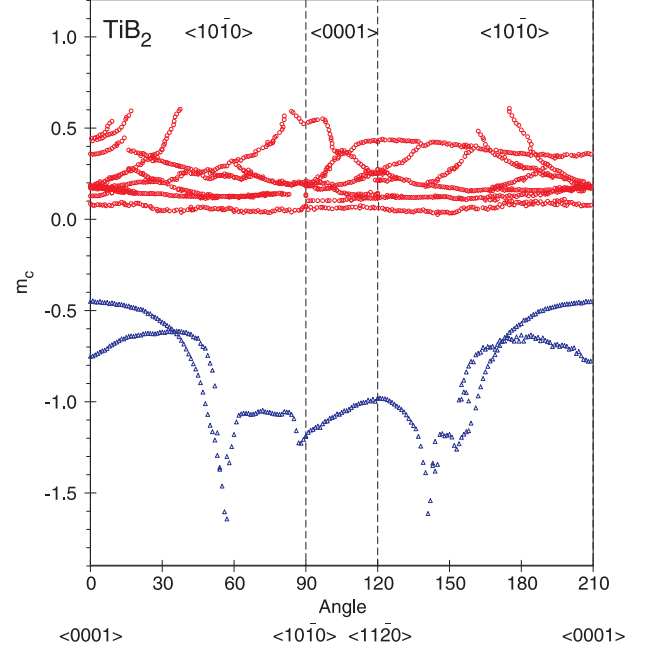


FIG. 16: (Color online) The calculated angular dependence of the cyclotron masses for the electron Fermi surface (red open circles) and the hole Fermi surface (blue open triangles) in the compound TiB_2 .

E. Phonon spectra

The unit cell of TB_2 ($\text{T}=\text{Zr}, \text{Ti}$) contains three atoms, which give in general case a nine phonon branches. Figure 17 shows theoretically calculated phonon density of state for ZrB_2 and TiB_2 . The DOS for both ZrB_2 and TiB_2 can be separated into three distinct regions. Based on our analysis of relative directions of eigenvectors for each atom in unit cell, we find that the first region (with a peak in phonon DOS at 29 meV in ZrB_2 and 37.5 meV in TiB_2) is dominated by the motion of the transition-metal atoms Zr and Ti, respectively. This region belongs to the acoustic phonon modes. The shift of the first region in the phonon DOS towards lower frequencies for ZrB_2 in comparison to TiB_2 is due to the higher mass of Zr. The second wide region (60-80 meV) results from the coupled motion of Zr(Ti) and the two B atoms in the unit cell. The E_{1u} , A_{2g} , B_{1g} phonon modes (see Table I) lie in this area. The phonon DOS in the third region extends from 88 meV to 103 meV in ZrB_2 and from 105 meV to 115 meV in TiB_2 . This is due to the movement of boron atoms and is expected since boron is lighter than transition metal atoms. The covalent character of the B-B bonding is also crucial for the high frequency of phonons. The in-plane E_{2g} mode belongs to this region. The second and third regions represent optical phonon modes in crystals. The most significant feature in the phonon DOS is a gap around 40 to 60 meV for both ZrB_2 and TiB_2 . This gap is a consequence of the large

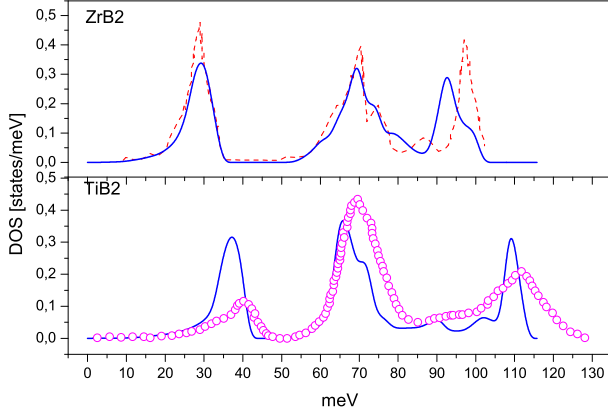


FIG. 17: (Color online) Theoretically calculated phonon density of states (full blue lines) for ZrB₂ and TiB₂ and experimentally measured one for TiB₂³² (open circles). Dashed red line presents the calculated phonon DOS of ZrB₂ by Deligoz *et al.* [50].

TABLE I: Theoretically calculated phonon frequencies (in meV) in the Γ symmetry point for ZrB₂ and TiB₂ and experimentally measured ones for TiB₂³² as well as calculated phonon frequencies in ZrB₂ calculated by Deligoz *et al.* Ref. [50].

Compound	reference	E_{1u}	A_{2g}	B_{1g}	E_{2g}
ZrB ₂	our results	58.70	63.26	71.0	99.70
	Ref. [50]	60.61	63.49	67.76	98.45
TiB ₂	our results	63.0	63.5	69.1	110.0
	Ref. [32]	65.5	66.4	70.0	112.8

mass difference, which leads to decoupling of transition metal and boron vibrations.

The TiB₂ phonon DOS was measured using inelastic neutron scattering experiments in Ref. 32. Our results are in good agreement with the experiment (see Fig. 17, lower panel). The small discrepancy in the positions of main peaks for TiB₂ does not exceed accuracy of calculation.

Currently, there are no data concerning the experimentally measured phonon DOS in ZrB₂. So we compare our results with theoretically calculated phonon DOS by Deligoz *et al.*⁵⁰ (Fig. 17, upper panel). Calculations of these authors were based on the density functional formalism and generalized gradient approximation. They used the Perdew-Burke-Ernzerhof functional⁷⁴ for the exchange-correlation energy as it is implemented in the SIESTA code.^{75,76} This code calculates the total energies and atomic Hellmann-Feynman forces using a linear combination of atomic orbitals as the basis set. The basis set consists of finite range pseudoatomic orbitals of the Sankey-Niklewsky type⁷⁷ generalized to include multiplezeta decays. The interactions between electrons and core ions are simulated with the separable Troullier-Martins⁷⁸ normconserving pseudopotentials. In other words, they used the so-called "frozen phonon" tech-

nique and built an optimized rhombohedral supercell with 36 atoms. This method is inconvenient for calculating phonon spectra for small \mathbf{q} -points as well as for compounds with large number of atoms per unit cell. There is a very good agreement between our calculations and the results of Deligoz *et al.*⁵⁰ in a shape and energy position of two first low energy peaks in the phonon DOS. There is only a low energy shift of the third peak by ~ 5 meV in our calculations in comparison with results of Deligoz *et al.*⁵⁰ (see also Table I).

F. Electron-phonon interaction

Figure 18 shows theoretically calculated Eliashberg functions for ZrB₂ and TiB₂. We find no significant difference in the shape and energy position of major peaks between phonon DOS values and electron-phonon coupling functions in these compounds. Therefore, we can conclude that electron-phonon Eliashberg function is mostly defined by the shape of phonon DOSs in ZrB₂ and TiB₂. There are no regions with unusually high electron-phonon interaction and phonon dispersion curves do not contain any soft modes which might be indicative of the possible superconductivity in these borides. By integrating the Eliashberg function using equation (8), we estimate the average electron-phonon interaction constant to be $\lambda_{e-ph}=0.14$ for ZrB₂. A similar result was obtained earlier by Singh⁴² ($\lambda=0.15$). Drechsler *et al.*⁴³ estimated the value of the dHvA orbit averaged el-ph coupling constant to be $\lambda \leq 0.1$. A weak electron-phonon coupling strength of $\lambda \sim 0.1$ was derived from both the comparison of the calculated density of states at the Fermi level and specific heat data (Fuchs *et al.*⁷⁹), and by point-contact measurements ($\lambda_{PC}=0.06$ ³³).

Figure 18 (upper panel) represents the PC electron-phonon interaction function for ZrB₂ in comparison with the theoretically calculated Eliashberg function. Results closely agree in the energy positions of major peaks. However, the experimental PC function displays a monotonically decreasing peak amplitude (as we move along the energy scale in the high-energy direction). As a consequence, the coupling PC constant $\lambda_{PC}=0.06$ is less than that obtained from the integration of the Eliashberg function ($\lambda_{e-ph}=0.14$). The disagreement might be explained by the fact that PC and the Eliashberg functions have a slightly different nature. First, the kinematic restriction of electron scattering processes in a PC is taken into account by a factor $K = \frac{1}{2}(1 - \theta \tan \theta)$, where θ is the angle between initial and final momenta of scattered electrons (for the Eliashberg function, the corresponding factor $K=1$). Therefore in PC spectra the large angle ($\theta \rightarrow \pi$) backscattering processes are dominated. The second reason for suppressing high-energy peaks in the PC function is a deviation from the ballistic electron flow in point-contact spectroscopy. (PC spectra can not be described in the framework of ballistic regime for a high-energy phonon area).³³

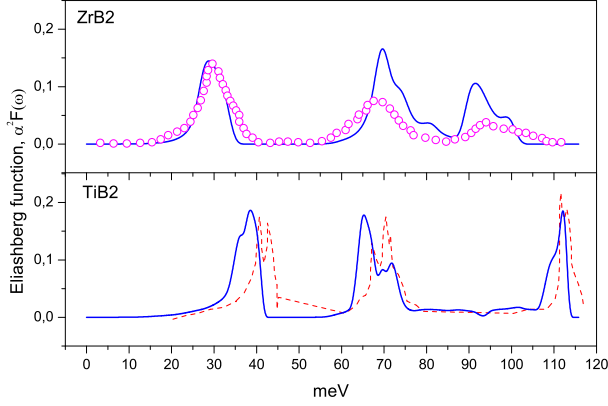


FIG. 18: (Color online) The theoretically calculated Eliashberg function $\alpha F(\omega)$ of ZrB_2 and TiB_2 (full blue lines) and experimentally measured point contact spectral function³³ (open circles) for ZrB_2 . Dashed red line presents Eliashberg function of TiB_2 calculated by Heid *et al.* Ref. [32].

For TiB_2 we again obtain a small value of the electron-phonon constant $\lambda_{e-ph}=0.15$. Due to absence of the experimentally measured electron-phonon spectral function in TiB_2 we compare our calculations with theoretical results obtained by Heid³² who used the mixed basis pseudopotential method.^{80,81} There is relatively good agreement between our calculations and Heid's results for the energy position and shape of the peaks (Fig. 18). The first two major low energy peaks of the Eliashberg function are slightly shifted towards the smaller energies in comparison with the results of Heid.³²

G. Electrical resistivity

In the pure metals (excluding low-temperature region), the electron-phonon interaction is the dominant factor governing electrical conductivity of the substance. Using lowest-order variational approximation, the solution for the Boltzmann equation gives the following formula for the temperature dependence of $\rho_I(T)$:

$$\rho_I(T) = \frac{\pi \Omega_{cell} k_B T}{N(\epsilon_F) \langle v_I^2 \rangle} \int_0^\infty \frac{d\omega}{\omega} \frac{\xi^2}{\sinh^2 \xi} \alpha_{tr}^2 F(\omega), \quad (10)$$

where, the subscript I specifies the direction of the electrical current. In our work, we investigate two direction: $[0001]$ (c-axis or z direction) and $[10\bar{1}0]$ (a-axis or x-direction). $\langle v_I^2 \rangle$ is the average square of the I component of the Fermi velocity, $\xi = \omega/2k_B T$.

Mathematically, the transport function $\alpha_{tr} F(\omega)$ differs from $\alpha F(\omega)$ only by an additional factor $[1 - v_I(\mathbf{k})v_I(\mathbf{k}')/\langle v_I^2 \rangle]$, which preferentially weights the backscattering processes.

Formula (10) remains valid in the range $\Theta_{tr}/5 < T < 2\Theta_{tr}$ ⁶⁶ where:

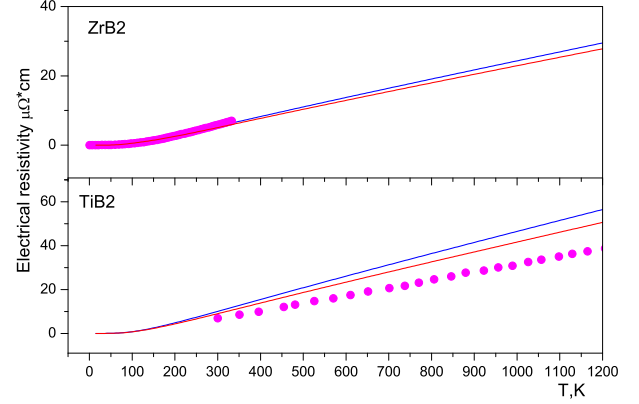


FIG. 19: (Color online) Theoretically calculated for the $\langle 0001 \rangle$ direction (blue curves) and the basal $\langle 10\bar{1}0 \rangle$ direction (red curves) and experimentally measured temperature dependence of electrical resistivity of ZrB_2 ⁸² (upper panel) and TiB_2 ⁸² (lower panel).

$$\Theta_{tr} \equiv \langle \omega^2 \rangle_{tr}^{1/2}, \quad (11)$$

$$\langle \omega^2 \rangle_{tr} = \frac{2}{\lambda_{tr}} \int_0^\infty \omega \alpha_{tr}^2 F(\omega) d\omega, \quad (12)$$

$$\lambda_{tr} = 2 \int_0^\infty \alpha_{tr}^2 F(\omega) \frac{d\omega}{\omega}, \quad (13)$$

The low-temperature electrical resistivity is the result of electron-electron interaction, size effects, scattering on impurities, etc., however, for high temperatures it is necessary to take into account the effects of anharmonicity and the temperature smearing of the Fermi surface. The $\Theta_{tr}=604.8$ K and 646.19 K for ZrB_2 and TiB_2 , respectively.

Figure 19 represents the experimental data for monocrystalline ZrB_2 ⁸² as well as our calculations (upper panel). No evidence of anisotropy of the electrical resistivity was found experimentally. Our theoretical calculations also show quite small anisotropically behavior of the electrical resistivity in ZrB_2 (compare red and blue curves in Fig. 19, upper panel). There is a good agreement between our calculations and experimentally measured results in the region up to 350 K.

We found that the anisotropy of the electrical resistivity in TiB_2 (Fig. 19, lower panel) is larger than it was in ZrB_2 . Our theoretical results slightly exceed experimental data,⁸² especially at high temperatures. This is due to using in our calculations the lowest-order variational approximation in solution of the Boltzmann equation which gives upper limit for the electrical resistivity.^{65,83}

IV. SUMMARY

We have studied the electronic structure and physical properties of ZrB₂ and TiB₂ using a full potential linear muffin-tin orbital method. We investigated the electron and phonon subsystems as well as the electron-phonon interaction in these compounds. The theory shows good agreement with experimentally measured x-ray absorption spectra at the B and Ti *K* and Zr *M*_{2,3} edges. Agreement between the experiment and the theory in optical spectra of ZrB₂ is also good. We found that the major peak in the $\epsilon_2(\omega)$ of ZrB₂ around 1 eV is mostly determined by the 5 \rightarrow 6 interband transitions along Γ –A and A–L symmetry directions.

We investigated the Fermi surface, angle dependence of the cyclotron masses, and extremal cross sections of the Fermi surface of ZrB₂ and TiB₂ in details. Theoretical calculations show a ring-like electron FS in ZrB₂ around the *K* symmetry point and a wrinkled dumbbell-like hole FS at the A point. TiB₂ has a smaller FS than ZrB₂. Theory reproduces the experimentally measured dHvA frequencies in both the ZrB₂ and TiB₂ reasonably well. We found that masses for low-frequency oscillations α , β , γ , and δ are less than $0.2m_0$. Masses for high-frequency oscillations ϵ , ν , μ , and ζ are large. We discover new branches σ both in ZrB₂ and TiB₂ which did not detected experimentally. Theoretical calculations closely reproduce the angle dependence of the extremal cross sections of high frequency orbits ϵ , μ , and ζ in ZrB₂. Similar orbits appeared in the theoretical results for TiB₂, but not detected experimentally. The cyclotron masses for these orbits in TiB₂ are much higher than the corresponding orbits in ZrB₂ (compare Figs. (15) and (16)). It could be one of the reasons why they have not been observed

in the dHvA measurements.²⁰

Calculated phonon spectra and phonon DOSs for both ZrB₂ and TiB₂ are in good agreement with experimental results as well as previous calculations. The Elishberg function of electron-phonon interaction in ZrB₂ is in good agreement with the experimentally measured point contact spectral function for both the position and the shape of the major peaks. We did not find regions with high electron-phonon interaction or phonon dispersion curves with soft modes in either ZrB₂ or TiB₂. This is in agreement with the fact that no trace of superconductivity was found in these borides. The averaged electron-phonon interaction constant was found to be rather small $\lambda_{e-ph}=0.14$ and 0.15 for ZrB₂ and TiB₂, respectively. We calculated the temperature dependence of the electrical resistivity in ZrB₂ and TiB₂ in the lowest-order variational approximation of the Boltzmann equation. We found rather small anisotropical behavior of the electrical resistivity in ZrB₂ to be in good agreement with experimental observation. We found that the anisotropy of electrical resistivity in TiB₂ is larger than it is in ZrB₂.

Acknowledgments

This work was carried out at the Ames Laboratory, which is operated for the U.S. Department of Energy by Iowa State University under Contract No. DE-AC02-07CH11358. This work was supported by the Director for Energy Research, Office of Basic Energy Sciences of the U.S. Department of Energy. This work was also supported by the National Academy of Sciences of Ukraine in the framework of the State Target Scientific and Technology Program of Implementation and Application of Grid Technologies for 2009-2013. V.N.A. gratefully acknowledges the hospitality during his stay at Ames Laboratory.

-
- ¹ K. Upadhyaya, J.-M. Yang, and W. P. Hoffmann, Am. Ceram. Soc. Bull. **76**, 51 (1997).
 - ² W. G. Fahrenholtz, G. E. Hilmas, I. G. Talmy, and J. A. Zaykoski, J. Am. Ceram. Soc. **90**, 1347 (2007).
 - ³ C. Mroz, Am. Ceram. Soc. Bull. **73**, 141 (1994).
 - ⁴ A. S. Brown, Aerospace Am. **35**, 20 (1997).
 - ⁵ K. Kuwabara, Bull. Ceram. Soc. Jpn. **37**, 267 (2002).
 - ⁶ S. Norasetthekul, P. T. Eubank, W. L. Bradley, B. Bozkurt, and B. Stucker, J. Mater. Sci. **34**, 1261 (1999).
 - ⁷ X. Li, M. H. Manghnani, L. C. Ming, and D. E. Grady, J. Appl. Phys. **80**, 3860 (1996).
 - ⁸ R. G. Munro, J. Res. Natl. Inst. Stand. Technol. **105**, 709 (2000).
 - ⁹ J. Nagamatsu, N. Nakagawa, T. Muranaka, Y. Zenitani, and J. Akimitsu, Nature (London) **410**, 63 (2001).
 - ¹⁰ V. A. Gasparov, N. S. Sidorov, I. I. Zverkova, and M. P. Kulakov, JETP Lett. **73**, 532 (2001).
 - ¹¹ D. P. Young, P. W. Adams, J. Y. Chan, and F. R. Fronczek, preprint cond-mat/0104063 (2001).
 - ¹² C. Buzea and T. Yamashita, Supercond. Sci. Technol. **14**, R115 (2001).
 - ¹³ V. A. Gasparov, M. P. Kulakov, N. S. Sidorov, I. I. Zverkova, V. B. Filipov, A. B. Lyashenko, , and Y. B. Paderno, JETP Letters **80**, 330 (2004).
 - ¹⁴ B. Fisher, K. B. Chashka, L. Patlagan, and G. M. Reisner, Physica C **384**, 1 (2003).
 - ¹⁵ V. A. Gasparov and A. Suslov, AIP Conf. Proc. **850**, 637 (2006).
 - ¹⁶ J. W. Zimmermann, G. E. Hilmas, , and W. G. Fahrenholtz, J. Am. Ceram. Soc. **91**, 1405 (2008).
 - ¹⁷ L. Zhang, D. A. Pejakovic, and J. Marschall, J. Am. Ceram. Soc. **94**, 2562 (2011).
 - ¹⁸ T. Tanaka, Y. Ishikawa, E. Bannai, and S. Kawai, Solid State Commun. **26**, 879 (1978).
 - ¹⁹ Y. Ishizawa and T. Tanaka, Inst. Phys. Conf. Ser. **75**, 29 (1986).
 - ²⁰ T. Tanaka and Y. Ishikawa, J. Phys. C: Solid St. Phys. **13**, 6671 (1980).
 - ²¹ V. B. Pluzhnikov, I. V. Svechkarov, A. V. Dukhnenko, A. V. Levchenko, V. B. Filippov, and A. Chopnik, Low Temp. Phys. **33**, 350 (2007).
 - ²² R. C. Linton, Thin Solid Films **20**, 17 (1974).
 - ²³ R. Roucka, V. R. D'Costa, Y.-J. An, M. Canonico, J. Kouvetakis, J. Menendez, and A. V. G. Chizmeshya, Chem

- Mater **20**, 1431 (2008).
- ²⁴ R. Roucka, Y.-J. An, A. V. G. Chizmeshya, V. D'Costa, J. Tolle, J. Menendez, and J. Kouvetakis, Solid-State Electronics **52**, 1687 (2008).
 - ²⁵ K. Lie, R. Brydson, and H. Davock, Phys. Rev. B **59**, 5361 (1999).
 - ²⁶ K. Lie, R. Hoier, and R. Brydson, Phys. Rev. B **61**, 1786 (2000).
 - ²⁷ H. Ihara, M. Hirabayashi, and H. Nakagawa, Phys. Rev. B **16**, 726 (1977).
 - ²⁸ S. Tsuda, R. Eguchi, A. Kosuge, T. Yokoya, A. Fukushima, S. Shin, A. Chainani, S. Otani, Y. Takano, K. Togano, et al., Physica C **392–396**, 259 (2003).
 - ²⁹ G. E. Grechnev, A. V. Fedorchenko, A. V. Logosha, A. S. Panfilov, I. V. Svechkarov, V. B. Filippov, A. B. Lyashchenko, and A. V. Evdokimova, J. Appl. Crystallogr. **481**, 75 (2009).
 - ³⁰ A. V. Fedorchenko, G. E. Grechnev, A. S. Panfilov, A. V. Logosha, I. V. Svechkarov, V. B. Filippov, A. B. Lyashchenko, and A. V. Evdokimova, Low Temp. Phys. **35**, 82 (2009).
 - ³¹ C. S. Lue and W. J. Lai, Phys. status solidi B **242**, 1108 (2005).
 - ³² R. Heid, B. Renker, H. Schober, P. Adelman, D. Ernst, and K. P. Bohnen, Phys. Rev. B **67**, 180510(R) (2003).
 - ³³ Y. G. Naidyuk, O. E. Kvitnitskaya, I. K. Yanson, S.-L. Drechsler, G. Behr, and S. Otani, Phys. Rev. B **66**, 140301(R) (2002).
 - ³⁴ D. L. Johnson, B. N. Harmon, and S. H. Liu, J. Chem. Phys. **73**, 1898 (1980).
 - ³⁵ J. K. Burdett, E. Canadell, and G. J. Miller, J. Am. Chem. Soc. **108**, 6561 (1986).
 - ³⁶ V. M. Anishchik and N. N. Dorozhkin, Phys. status solidi B **160**, 173 (1990).
 - ³⁷ P. Vajeeston, P. Ravindran, C. Ravil, and R. Asokamani, Phys. Rev. B **63**, 045115 (2001).
 - ³⁸ H. Rosner, J. M. An, W. E. Pickett, , and S.-L. Drechsler, Phys. Rev. B **66**, 024521 (2002).
 - ³⁹ P. de la Mora, M. Castro, and G. Tavizon, J. Solid State Chem. **169**, 168 (2002).
 - ⁴⁰ I. Shein and A. Ivanovskii, Phys. Solid. State **44**, 1833 (2002).
 - ⁴¹ C. Paduani, Phys. status solidi B **240**, 574 (2003).
 - ⁴² P. P. Singh, Phys. Rev. B **69**, 094519 (2004).
 - ⁴³ S.-L. D. aand H. Rosner, I. Opahle, S. Shulga, and H. Eschrig, Physica C **408–410**, 104 (2004).
 - ⁴⁴ S. T. Mahmud, Islam, and F. N. Islam, J. Phys.: Condens. Matter **16**, 2335 (2004).
 - ⁴⁵ B. Mouffok, H. Feraoun, and H. Aourag, Materials Letters **60**, 1433 (2006).
 - ⁴⁶ Y. Han, Y. Dai, D. Shu, J. Wang, and B. Sun, J. Appl. Crystallogr. **438**, 327 (2007).
 - ⁴⁷ X. Zhang, X. Luo, J. Han, J. Li, and W. Han, Comput. Mat. Sci. **44**, 411 (2008).
 - ⁴⁸ E. Deligoz, K. Colakoglu, and Y. Ciftci, Solid State Commun. **149**, 1843 (2009).
 - ⁴⁹ X. Zhang, X. Luo, J. Li, J. Han, W. Han, and C. Hong, Comput. Mat. Sci. **46**, 1 (2009).
 - ⁵⁰ E. Deligoz, K. Colakoglu, and Y. Ciftci, Solid State Commun. **150**, 405 (2010).
 - ⁵¹ H. Fu, M. Teng, X. Hong, and Y. L. aand T. Gao, Physica B **405**, 846 (2010).
 - ⁵² V. Milman, B. Winkler, and M. I. J. Probert, J. Phys.: Condens. Matter **13**, 2233 (2005).
 - ⁵³ N. Kaur, R. Mohan, N. K. Gaur, and R. K. Singh, Physica B **404**, 1607 (2009).
 - ⁵⁴ V. Milman and M. Warren, J. Phys.: Condens. Matter **13**, 5585 (2001).
 - ⁵⁵ C. A. Perottoni, A. S. Pereira, and J. A. H. da Jornada, J. Phys.: Condens. Matter **12**, 7205 (2000).
 - ⁵⁶ P. E. van Camp and D. E. van Doren, High Pressure Res. **13**, 335 (2005).
 - ⁵⁷ F. Peng, H.-Z. Fu, and X.-L. Cheng, Physica B **400**, 83 (2007).
 - ⁵⁸ T. Oguchi, J. Phys. Soc. Jpn. **71**, 1495 (2002).
 - ⁵⁹ W. S. Chu, Z. Y. Wu, S. Agrestini, A. Binamconi, A. Marcelli, and W. H. Liu, **19**, 2386 (2005).
 - ⁶⁰ V. Antonov, B. Harmon, and A. Yaresko, *Electronic Structure and Magneto-Optical Properties of Solids* (Kluwer, Dordrecht, 2004).
 - ⁶¹ R. Kubo, J. Phys. Soc. Jpn. **12**, 570 (1957).
 - ⁶² C. S. Wang and J. Callaway, Phys. Rev. B **9**, 4897 (1974).
 - ⁶³ V. N. Antonov, A. I. Bagljuk, A. Y. Perlov, V. V. Nemoshkalenko, V. N. Antonov, O. K. Andersen, and O. Jepsen, Low Temp. Phys. **19**, 494 (1993).
 - ⁶⁴ G. Y. Guo, H. Ebert, W. M. Temmerman, and P. J. Durham, Phys. Rev. B **50**, 3861 (1994).
 - ⁶⁵ P. B. Allen, Phys. Rev. B **6**, 2577 (1972).
 - ⁶⁶ S. Y. Savrasov and D. Y. Savrasov, Phys. Rev. B **54**, 16470 (1996).
 - ⁶⁷ M. Stueemke and G. Petzow, Zeitschrift fuer Metallkunde **66**, 292 (1975).
 - ⁶⁸ S. Otani and Y. Ishizawa, J. Crystal Growth **140**, 451 (1994).
 - ⁶⁹ J. Perdew and Y. Wang, Phys. Rev. B **45**, 13244 (1992).
 - ⁷⁰ P. E. Blöchl, O. Jepsen, and O. K. Andersen, Phys. Rev. B **49**, 16223 (1994).
 - ⁷¹ A. Pasturel, C. Colinet, and P. Hichter, Physica B **132**, 177 (1985).
 - ⁷² J. Piper, J. Phys. Chem. Solids **27**, 1907 (1966).
 - ⁷³ S. H. Liu, L. Kopp, W. B. England, and H. W. Myron, Phys. Rev. B **11**, 3463 (1975).
 - ⁷⁴ M. E. J. Perdew, K. Burke, Phys. Rev. Lett. **77**, 3865 (1996).
 - ⁷⁵ J. S. P. Ordejon, E. Artacho, Phys. Rev. B (Rapid Comm.) **53**, R10441 (1996).
 - ⁷⁶ J. M. Soler, E. Artacho, J. D. Gale, A. Garca, J. Junquera, P. Ordejon, and D. Sanchez-Portal, J. Phys.: Condens. Matter **14**, 2745 (2002).
 - ⁷⁷ D. N. O.F. Sankey, Phys. Rev. B **40**, 3979 (1989).
 - ⁷⁸ J. M. N. Troullier, Phys. Rev. B **43**, 1993 (1991).
 - ⁷⁹ G. Fuchs, S.-L. Drechsler, K.-H. Müller, A. Handstein, S. V. Shulga, G. Behr, A. Gümbel, J. Eckert, K. Nenkov, V. N. Narozhnyi, et al., J. Low Temper. Phys. **131**, 1159 (2003).
 - ⁸⁰ R. H. K.P. Bohnen and B. Renker, Phys. Rev. Lett. **86**, 5771 (2001).
 - ⁸¹ K. B. R. Heid and B. Renker, Adv. Solid State Phys. **42**, 293 (2002).
 - ⁸² A. D. McLeod, J. S. Haggerty, and D. R. Sadoway, J. American Ceramis Society **67**, No11, 705 (1984).
 - ⁸³ J. M. Ziman, *Electrons and Phonons* (Oxford University Press, Oxford, 1960).